



# A SURVEY OF LUMINOUS HIGH-REDSHIFT QUASARS WITH SDSS AND WISE. II. THE BRIGHT END OF THE QUASAR LUMINOSITY FUNCTION AT $z \sim 5$

JINYI YANG<sup>1,2</sup>, FEIGE WANG<sup>1,2</sup>, XUE-BING WU<sup>1,3</sup>, XIAOHUI FAN<sup>2,3</sup>, IAN D. MCGREER<sup>2</sup>,  
FUYAN BIAN<sup>4,9</sup>, WEIMIN YI<sup>5,6</sup>, QIAN YANG<sup>1,2</sup>, YANLI AI<sup>7</sup>, XIAOYI DONG<sup>1</sup>, WENWEN ZUO<sup>8</sup>,  
RICHARD GREEN<sup>2</sup>, LINHUA JIANG<sup>3</sup>, SHU WANG<sup>1</sup>, RAN WANG<sup>3</sup>, AND MINGHAO YUE<sup>1</sup>

<sup>1</sup>Department of Astronomy, School of Physics, Peking University, Beijing 100871, China

<sup>2</sup>Steward Observatory, University of Arizona, 933 North Cherry Avenue, Tucson, AZ 85721, USA

<sup>3</sup>Kavli Institute for Astronomy and Astrophysics, Peking University, Beijing 100871, China

<sup>4</sup>Research School of Astronomy and Astrophysics, Australian National University, Weston Creek, ACT 2611, Australia

<sup>5</sup>Yunnan Observatories, Chinese Academy of Sciences, Kunming 650011, China

<sup>6</sup>Key Laboratory for the Structure and Evolution of Celestial Objects, Chinese Academy of Sciences, Kunming 650011, China

<sup>7</sup>School of Astronomy and Space Science, Sun Yat-Sen University, Guangzhou 510275, China

<sup>8</sup>Shanghai Astronomical Observatory, Chinese Academy of Sciences, Shanghai 200030, China

Received 2016 February 14; revised 2016 June 25; accepted 2016 July 14; published 2016 September 20

## ABSTRACT

This is the second paper in a series on a new luminous  $z \sim 5$  quasar survey using optical and near-infrared colors. Here we present a new determination of the bright end of the quasar luminosity function (QLF) at  $z \sim 5$ . Combining our 45 new quasars with previously known quasars that satisfy our selections, we construct the largest uniform luminous  $z \sim 5$  quasar sample to date, with 99 quasars in the range of  $4.7 \leq z < 5.4$  and  $-29 < M_{1450} \leq -26.8$ , within the Sloan Digital Sky Survey (SDSS) footprint. We use a modified  $1/V_a$  method including flux limit correction to derive a binned QLF, and we model the parametric QLF using maximum likelihood estimation. With the faint-end slope of the QLF fixed as  $\alpha = -2.03$  from previous deeper samples, the best fit of our QLF gives a flatter bright end slope  $\beta = -3.58 \pm 0.24$  and a fainter break magnitude  $M_{1450}^* = -26.98 \pm 0.23$  than previous studies at similar redshift. Combined with previous work at lower and higher redshifts, our result is consistent with a luminosity evolution and density evolution model. Using the best-fit QLF, the contribution of quasars to the ionizing background at  $z \sim 5$  is found to be 18%–45% with a clumping factor  $C$  of 2–5. Our sample suggests an evolution of radio loud fraction with optical luminosity but no obvious evolution with redshift.

**Key words:** galaxies: active – galaxies: high-redshift – quasars: general

## 1. INTRODUCTION

Quasars comprise the most luminous class of non-transient objects in the universe. Characterizing their population and evolution is the critical tool to directly constrain the formation and evolution of supermassive black holes (SMBHs) across cosmic time. The fundamental way to characterize these objects is through the evolution of their number densities with luminosity and redshift, namely the quasar luminosity function (QLF). The QLF and its cosmological evolution have been a key focus of quasar studies for half a century. Schmidt (1968) first determined the evolution of the quasar population and found the first evidence for a significant increase of the quasar number density with redshift in both radio and optical bands. More recently, based on measurements of the QLF from several successful surveys, such as the 2dF Quasar Redshift Survey (Boyle et al. 2000; Croom et al. 2004), COMBO-17 (Wolf et al. 2003), the 2dF-SDSS LRG and QSO survey (2SLAQ; Richards et al. 2005), the SDSS Faint Quasar Survey (Jiang et al. 2006), the VIMOS-VLT Deep Survey (VVDS; Bongiorno et al. 2007), SDSS and 2SLAQ (Croom et al. 2009), and BOSS DR9 (Ross et al. 2013), the QLF, especially in optical bands, has been well characterized at low to intermediate redshifts. The QLF can be parameterized with a double power-law shape and pure luminosity evolution for quasars at redshifts up to  $z = 2$  (Boyle et al. 2000; Croom et al. 2004). The bright end slope at low redshift, the effect of

“cosmic downsizing,” and the density peak of quasars at  $2 < z < 3$  (Brown et al. 2006; Jiang et al. 2006; Richards et al. 2006; Croom et al. 2009) have been confirmed by many subsequent investigations. The measurements based on large samples from BOSS yield a QLF evolution best fit by a luminosity evolution and density evolution (LEDE) model at  $2 < z < 3.5$  (Ross et al. 2013). In their work, the bright end slope does not evolve with redshift and is different from the result of Richards et al. (2006), which suggested a flatter bright end slope at high redshift than that at low redshift. To better determine the evolution of QLF parameters, a wider redshift range is needed.

Toward higher redshift, quasars are important tracers of the structure and evolution of the early universe, the evolution of the intergalactic medium (IGM), the growth of SMBHs and co-evolution of SMBHs and host galaxies at early epochs. Observations of the Gunn–Peterson effect using absorption spectra of quasars at  $z \gtrsim 5.7$  have established  $z \sim 6$  as the end of cosmic reionization, when the IGM is rapidly transforming from largely neutral to completely ionized (Fan et al. 2006). Becker et al. (2015) find evidence for UV background fluctuations at  $z \sim 5.7$  in excess of predictions from a single mean-free-path model, which indicates that reionization is not fully complete at that redshift. McGreer et al. (2015) suggest that reionization is just completing at  $z \sim 6$ , possibly with a tail to  $z \sim 5.5$ . Therefore, in the post-reionization epoch, the QLF at  $z \gtrsim 5$  is needed to estimate the contribution of quasars to the ionizing background during and after the reionization epoch.

<sup>9</sup> Stromlo Fellow.

Although quasars are not likely to be the dominant source of ionizing photons (Fan et al. 2001a; Willott et al. 2010; McGreer et al. 2013), their exact contribution is still highly uncertain. In addition,  $z \sim 5$  quasar absorption spectra can be used to constrain the physical conditions of the IGM in this key redshift range, and provide the basic boundary conditions for models of reionization, such as the evolution of IGM temperature, photon mean-free path, metallicity and the impact of helium reionization (Bolton et al. 2012).

However, high-redshift quasars are very rare, especially at  $z > 5$ . Although more than 300,000 quasars are known, only  $\sim 200$  of them are at  $z > 5$ . Therefore, QLF measurements at high redshift still have large uncertainties. From the combination of SDSS DR7 quasars and the Stripe 82 (S82) faint quasar sample, McGreer et al. (2013) provided the most complete measurement of the  $z \sim 5$  QLF so far, especially at the faint end. A factor of two greater decrease in the number density of luminous quasars from  $z = 5$  to 6 than that from  $z = 4$  to 5 was claimed (McGreer et al. 2013, hereafter M13). However, their work focused on the faint end; there are only eight quasars with  $M_{1450} < -27.3$  in the sample.

A survey described in this series of papers is aimed at finding more luminous quasars at  $4.7 < z < 5.5$ , which allows a better determination of the bright end QLF and a better constraint on the quasar evolution model at high redshift. Wang et al. (2016, hereafter Paper I) presented a new selection using SDSS and the *Wide-field Infrared Survey Explorer* (WISE) optical/NIR colors. In this follow-up paper, we report our measurement of the bright end  $z \sim 5$  QLF using the quasar sample selected by the method presented in Paper I. The outline of our paper is as follows. In Section 2, we briefly review the quasar candidate selection and the spectroscopic observations of these candidates. The survey completeness will be presented in Section 3. In this section, we use a quasar color model (M13) to quantify our selection completeness and to correct the incompleteness due to the ALLWISE detection flux limit and spectral coverage. We then calculate the binned luminosity function and fit our data using a maximum likelihood estimator in Section 4. We also study the evolution of the QLF and compare our results with previous work in this section. In Section 5, we discuss the contribution of  $z \sim 5$  quasars to the ionizing background and the radio loud fraction of our quasar sample. We summarize our main results in Section 6. In this paper, we adopt a  $\Lambda$ CDM cosmology with parameters  $\Omega_\Lambda = 0.728$ ,  $\Omega_m = 0.272$ ,  $\Omega_b = 0.0456$ , and  $H_0 = 70 \text{ km s}^{-1} \text{ Mpc}^{-1}$  (Komatsu et al. 2009) for direct comparison with the result in M13. Photometric data from the SDSS are in the SDSS photometric system (Lupton et al. 1999), which is almost identical to the AB system at bright magnitudes; photometric data from ALLWISE are in the Vega system. All SDSS data shown in this paper are corrected for Galactic extinction.

## 2. A LARGE SAMPLE OF LUMINOUS QUASARS AT $z \sim 5$

### 2.1. Quasar Selection and Spectroscopic Observations

Our SDSS+WISE selection technique and spectroscopic follow-up observations were discussed in detail in Paper I. Here we briefly review the basic steps. At  $z \sim 5$ , most quasars are undetectable in the  $u$  band and  $g$  band because of the presence of strong Lyman limit systems, which are optically thick to the UV continuum radiation from quasars (Fan et al.

1999). The Ly $\alpha$  absorption systems also begin to dominate in the  $r$  band and Ly $\alpha$  emission moves to the  $i$  band. Therefore, the  $r - i/i - z$  color-color diagram was often used to select  $z \sim 5$  quasar candidates in previous studies (Fan et al. 1999; Richards et al. 2002; M13). However, with increasing redshift, the  $i - z$  color also becomes increasingly red and most  $z > 5.1$  quasars enter the M star locus in the  $r - i/i - z$  color-color diagram, which makes it difficult to find  $z > 5.1$  quasars with only the optical colors. Therefore, we added near-infrared colors from WISE photometry data in our selection. We used typical  $u$ ,  $g$  drop-out methods but more relaxed  $r - i/i - z$  cuts to select candidates from the SDSS DR10 database. Then we cross-matched our candidates with the ALLWISE database using a  $2''$  match radius and used  $z$ -W1/W1-W2 cuts to remove more star contaminations by the following criteria. The exact selection criteria are given in Paper I.

$$z - W1 > 2.5 \quad (1)$$

$$W1 - W2 > 0.5 \quad (2)$$

$$W1 < 17.0, \sigma_{W2} < 0.2 \quad (3)$$

$$z - W1 > 2.8 \text{ or } W1 - W2 > 0.7, \text{ if } i - z > 0.4. \quad (4)$$

We constructed our main luminous quasar candidate sample by limiting the SDSS  $z$ -band magnitudes to brighter than 19.5, and selected a total of 420 luminous  $z \sim 5$  quasar candidates. We removed 78 known quasars, one known dwarf and 231 candidates with suspicious detections, such as multiple peaked objects or being affected by bright star artifacts. We visually inspected images of each candidate and removed those 231 candidates. We selected 110 candidates with high image quality as our main candidate sample. Our spectroscopic follow-up campaign started in 2013 October. We observed 99 candidates from our main sample with the Lijiang 2.4 m telescope (LJT) and Xinglong 2.16 m telescope in China, the Kitt Peak 2.3 m Bok telescope and 6.5 m MMT telescope in the U.S., as well as the 2.3 m ANU telescope in Australia. 64 (64.6%) candidates have been identified as high-redshift quasars in the redshift range  $4.4 \lesssim z \lesssim 5.5$ . As discussed in Paper I, due to the serious contamination from M-type stars, there is a gap in the previously published quasar redshift distribution at  $5.2 < z < 5.7$  with only 33 published quasars in this redshift range. Among our 64 newly identified quasars from main candidates sample, 9 quasars are at  $5.2 < z < 5.7$ , which represents an increase of 27% in the number of known quasars in this redshift range. The details of spectroscopic observation and data reduction are also given in Paper I.

### 2.2. Quasar Sample

The redshifts of newly identified quasars are measured from Ly $\alpha$ , NV, OI/Si II, C II, Si IV, and C IV emission lines (any available) by an eye-recognition assistant for quasar spectra software (ASERA; Yuan et al. 2013). The typical redshift error is about 0.05 for Ly $\alpha$ -based redshift measurement and will be less for that based on more emission lines. We calculate  $M_{1450}$  in the AB system by fitting a power-law continuum  $f_\nu \sim \nu^{\alpha_\nu}$  to the spectrum for each quasar. We assume an average quasar UV continuum slope of  $\alpha_\nu = -0.5$  (Vanden Berk et al. 2001; see details in Paper I). Our 64 new quasars from the luminous quasar candidate sample are within the absolute magnitude range  $-29 < M_{1450} < -26.4$ . We calculate  $M_{1450}$  for previous known quasars using the same method. The known quasars are from the SDSS DR7 and DR12 quasar catalogs (Schneider

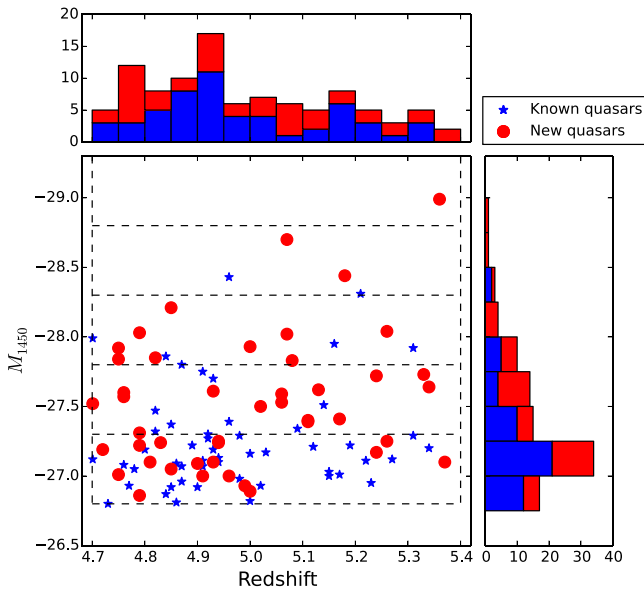


**Figure 1.** Redshift and  $M_{1450}$  distributions of both our newly identified luminous quasars (red dots) and known quasars (blue stars) at  $4.7 \lesssim z \lesssim 5.4$  and  $-29.3 \lesssim M_{1450} \lesssim -26.8$ . The known quasars are from the SDSS DR7 and DR12 quasar catalogs (Schneider et al. 2010; Pärís et al. 2016; McGreer et al. 2009; Schneider et al. 1991). This is the sample used for QLF measurement. The dashed lines represent the redshift and magnitude bins for determining the binned QLF. We use only one redshift bin.

et al. 2010; Pärís et al. 2016; McGreer et al. 2013; Schneider et al. 1991). When we removed the known quasars from our quasar candidate sample, we missed two known quasars. These two quasars from McGreer et al. (2009) and Schneider et al. (1991) were also spectroscopically observed by us, and thus we use our new spectra to do the  $M_{1450}$  calculation.

For the QLF determination, we define our sample of  $z \sim 5$  luminous quasars as follows.

1. Quasars in the redshift range  $4.7 \leq z < 5.4$ . Our selection criteria yield low completeness at redshifts lower than 4.7 or higher than 5.4. The former is caused by the drop of  $W1 - W2$  color (See Figure 3 in Paper I), and the latter is caused by our  $r - i/i - z$  limit. Therefore, we restrict our sample to the range of  $4.7 \leq z < 5.4$  (see details in Section 3.2).
2. Quasars in the luminosity range of  $M_{1450} \leq -26.8$ . Our selection criteria yield a low completeness in the region with  $z > 5$  and  $-26.8 < M_{1450} < -26.4$ . The mean completeness in this region is  $\sim 4\%$ . That is caused by our SDSS magnitude limit of  $z < 19.5$ . Therefore, we limit our sample to  $M_{1450} \leq -26.8$ .
3. Our selection covers the whole SDSS footprint without masked regions, which is a 14,555 square degree field.

Based on the criteria above, there are 45 newly identified quasars in the sample of Paper I and another 54 previously known quasars that satisfy our selection criteria. This is the final complete  $z \sim 5$  luminous quasar sample that we will use to determine the  $z \sim 5$  QLF. Figure 1 shows the redshift and  $M_{1450}$  distributions of both our newly identified luminous quasars and known quasars. Three of our new quasars are more luminous than any previously known quasars at  $z > 5$ . It is obvious that our discovery significantly expands the  $z \sim 5$

luminous quasar sample. Table 1 lists all 99 quasars in our sample used for the QLF determination.

### 3. SURVEY COMPLETENESS

In this section, we will discuss the incompleteness corrections. We limit our candidates to be brighter than 19.5 mag in the SDSS  $z$  band, the ALLWISE detection is not deep enough for all quasars in this magnitude range and its depth highly depends on sky position. Therefore, we first model the ALLWISE incompleteness caused by survey depth. We then correct for the incompleteness of our SDSS-ALLWISE color-color selection. Besides, there are 11 candidates that have not been observed, which leads to an incompleteness. For photometric completeness, we visually inspected images of each candidate. To see how many quasars will be missed in this step, we randomly selected 2000 SDSS images of point sources in the same magnitude range as our quasar candidates. We divided them into four groups and visually inspected the images. The fraction of rejected images is 2%–4% in each group. It is difficult to obtain a more accurate value of this incompleteness and this effect is much smaller than the error of QLF, thus image selection is not included in our incompleteness correction.

#### 3.1. Model ALLWISE Incompleteness

The magnitude limit of our main sample is SDSS  $z = 19.5$ , which is much brighter than the flux limit ( $5\sigma$ ) of the SDSS survey. Therefore, within our magnitude limit, the SDSS detections can be considered as complete. Our survey adds ALLWISE W1 and W2 photometric data into the selection, and thus we need to consider the detection incompleteness caused by the shallower ALLWISE detection limit. We correct this by using the ALLWISE detection completeness from the Explanatory Supplement to the AllWISE Data Release Products<sup>10</sup>, which is a function of frame coverage and flux in W1 and W2 bands respectively. Figure 2 represents the empirical models of 2D detection completeness in W1 and W2 bands. As shown, our sample limited with  $W1 < 17$  and  $\sigma_{W2} < 0.2$  will be effected slightly by the detection incompleteness at the faint end.

The ALLWISE coverage depends on the sky position. To take the position-dependence into account on completeness correction, we mapped the ALLWISE spatial surveying depth within the SDSS footprint. We first randomly generated  $\sim 1,220,000$  positions in the whole SDSS footprint and derived the ALLWISE coverage map in the SDSS footprint by matching( $1'$ ) positions to the nearest ALLWISE sources. A detection with coverage  $\leq 5$  could be contaminated by random pixel variations such as cosmic rays because they are at or below the threshold for ALLWISE statistically viable outlier detection and rejection. So we removed all positions with frame coverage  $\leq 5$ . There are only 269 (0.02%) positions with coverage  $\leq 5$ . Figure 3 shows the distributions of W1/W2 frame coverages in the whole SDSS footprint. The average coverage is 36 in both W1 and W2 bands. The 10% and 90% tile coverage in W1/W2 band are 23/22 and 56/56. We use our ALLWISE coverage map to correct the detection incompleteness (see details in Section 3.2).

<sup>10</sup> <http://wise2.ipac.caltech.edu/docs/release/allwise/>

**Table 1**  
 $z \sim 5$  Quasar Sample Used for QLF Measurement

Name	$r_{\text{SDSS}}$	$i_{\text{SDSS}}$	$z_{\text{SDSS}}$	W1	W2	Redshift	$M_{1450}$	Notes <sup>a</sup>
J000851.43+361613.49	21.45 ± 0.08	19.50 ± 0.02	19.20 ± 0.05	16.05 ± 0.05	15.37 ± 0.09	5.17	−27.41	Paper I
J001115.24+144601.80	19.48 ± 0.02	18.17 ± 0.02	18.03 ± 0.03	15.29 ± 0.04	14.69 ± 0.06	4.96	−28.43	DR12
J002526.84−014532.51	19.58 ± 0.02	18.03 ± 0.02	17.85 ± 0.02	14.80 ± 0.03	14.16 ± 0.05	5.07	−28.70	Paper I
J005527.19+122840.67	20.23 ± 0.03	18.71 ± 0.02	18.66 ± 0.04	15.45 ± 0.05	14.95 ± 0.09	4.70	−27.52	Paper I
J011614.30+053817.70	21.57 ± 0.09	19.87 ± 0.03	19.22 ± 0.06	16.37 ± 0.07	15.76 ± 0.13	5.33	−27.73	Paper I
J012247.35+121624.06	22.25 ± 0.14	19.37 ± 0.03	19.27 ± 0.06	15.59 ± 0.05	14.91 ± 0.07	4.79	−26.86	Paper I
J013127.34−032100.19	20.15 ± 0.04	18.46 ± 0.02	18.01 ± 0.03	14.58 ± 0.03	13.84 ± 0.04	5.18	−28.44	Paper I
J014741.53−030247.88	20.08 ± 0.03	18.53 ± 0.02	18.21 ± 0.02	14.86 ± 0.03	14.32 ± 0.05	4.75	−27.84	Paper I
J015533.28+041506.74	21.70 ± 0.10	19.97 ± 0.03	19.26 ± 0.06	16.33 ± 0.07	15.19 ± 0.10	5.37	−27.10	Paper I
J015618.99−044139.88	20.77 ± 0.04	19.10 ± 0.02	19.13 ± 0.05	15.36 ± 0.04	14.69 ± 0.06	4.94	−27.24	Paper I
J021624.16+230409.47	21.26 ± 0.06	19.78 ± 0.03	19.32 ± 0.06	16.56 ± 0.08	15.73 ± 0.15	5.26	−27.25	Paper I
J021736.76+470826.48	20.55 ± 0.05	18.96 ± 0.02	18.88 ± 0.05	15.76 ± 0.05	15.14 ± 0.08	4.81	−27.10	Paper I
J022055.59+473319.34	20.07 ± 0.03	18.34 ± 0.01	18.31 ± 0.03	15.19 ± 0.04	14.62 ± 0.06	4.82	−27.85	Paper I
J024601.95+035054.12	21.05 ± 0.05	19.28 ± 0.02	19.36 ± 0.05	16.67 ± 0.07	15.74 ± 0.14	4.96	−27.00	Paper I
J025121.33+033317.42	20.80 ± 0.04	19.04 ± 0.03	19.06 ± 0.05	15.64 ± 0.04	14.93 ± 0.07	5.00	−26.89	Paper I
J030642.51+185315.85	19.89 ± 0.03	17.96 ± 0.01	17.47 ± 0.02	14.31 ± 0.03	13.46 ± 0.04	5.36	−28.99	Paper I
J032407.69+042613.29	20.39 ± 0.04	19.03 ± 0.02	19.15 ± 0.06	15.72 ± 0.05	15.13 ± 0.09	4.72	−27.19	Paper I
J045427.96−050049.38	19.91 ± 0.03	18.59 ± 0.03	18.39 ± 0.03	15.09 ± 0.03	14.53 ± 0.05	4.93	−27.61	Paper I
J065330.25+152604.71	21.27 ± 0.06	19.48 ± 0.02	19.39 ± 0.07	16.65 ± 0.11	15.79 ± 0.16	4.90	−27.09	Paper I
J073103.13+445949.43	20.66 ± 0.04	19.06 ± 0.02	19.07 ± 0.05	15.82 ± 0.05	15.30 ± 0.09	4.98	−27.29	DR12
J073231.28+325618.33	20.26 ± 0.03	18.82 ± 0.01	18.62 ± 0.03	15.46 ± 0.04	14.92 ± 0.08	4.76	−27.60	Paper I
J074154.72+252029.65 <sup>b</sup>	20.49 ± 0.03	18.45 ± 0.02	18.36 ± 0.02	14.78 ± 0.03	13.81 ± 0.04	5.21	−28.31	McGreer2009
J074749.18+115352.46	20.44 ± 0.03	18.67 ± 0.02	18.27 ± 0.03	14.64 ± 0.03	13.79 ± 0.04	5.26	−28.04	Paper I
J075907.58+180054.71	20.95 ± 0.04	19.12 ± 0.02	19.11 ± 0.04	16.07 ± 0.07	15.39 ± 0.11	4.78	−27.05	DR12
J080306.19+403958.96	20.58 ± 0.04	18.88 ± 0.02	18.60 ± 0.03	15.28 ± 0.04	14.76 ± 0.06	4.79	−27.22	Paper I
J081333.33+350810.78	20.49 ± 0.03	18.97 ± 0.02	18.94 ± 0.04	15.79 ± 0.05	15.06 ± 0.08	4.92	−27.27	DR12
J082454.02+130216.98	21.36 ± 0.06	19.90 ± 0.03	19.43 ± 0.07	16.43 ± 0.08	15.86 ± 0.18	5.15	−27.03	DR12
J083832.31−044017.47	21.20 ± 0.06	19.62 ± 0.03	19.21 ± 0.07	15.58 ± 0.04	15.06 ± 0.08	4.75	−27.01	Paper I
J084631.53+241108.37	20.76 ± 0.03	19.15 ± 0.02	19.27 ± 0.04	15.66 ± 0.05	15.14 ± 0.12	4.73	−26.80	DR12
J085430.37+205650.84	21.99 ± 0.10	19.37 ± 0.03	19.38 ± 0.06	16.21 ± 0.07	15.17 ± 0.10	5.17	−27.01	DR12
J091543.64+492416.65	20.93 ± 0.05	19.57 ± 0.02	19.40 ± 0.06	16.41 ± 0.07	15.54 ± 0.10	5.19	−27.22	DR12
J094108.36+594725.76	20.56 ± 0.04	19.27 ± 0.02	19.28 ± 0.06	16.44 ± 0.06	15.88 ± 0.13	4.86	−26.81	DR12
J095707.68+061059.55	20.60 ± 0.03	19.21 ± 0.02	18.87 ± 0.04	16.18 ± 0.07	15.54 ± 0.13	5.14	−27.51	DR12
J100416.13+434739.12	20.95 ± 0.05	19.38 ± 0.02	19.31 ± 0.06	16.64 ± 0.08	16.11 ± 0.18	4.84	−26.87	DR12
J102622.88+471907.19	20.17 ± 0.03	18.73 ± 0.01	18.62 ± 0.04	15.58 ± 0.04	14.85 ± 0.06	4.93	−27.62	DR12
J104041.10+162233.87	20.50 ± 0.03	18.82 ± 0.07	18.75 ± 0.04	16.14 ± 0.06	15.19 ± 0.12	4.80	−27.19	DR12
J104242.41+310713.20	20.37 ± 0.04	18.98 ± 0.02	18.96 ± 0.05	16.18 ± 0.06	15.59 ± 0.12	4.70	−27.12	DR12
J104325.56+404849.49	20.70 ± 0.04	19.02 ± 0.02	19.09 ± 0.04	15.87 ± 0.05	15.06 ± 0.08	4.91	−27.07	DR12
J105020.41+262002.33	20.74 ± 0.04	19.39 ± 0.02	19.34 ± 0.06	16.38 ± 0.07	15.70 ± 0.14	4.86	−27.09	DR12
J105123.04+354534.31	20.23 ± 0.03	18.42 ± 0.02	18.56 ± 0.04	15.46 ± 0.04	14.84 ± 0.06	4.91	−27.75	DR12
J105322.99+580412.13	21.51 ± 0.05	19.80 ± 0.02	19.49 ± 0.05	16.89 ± 0.09	15.96 ± 0.13	5.27	−27.12	DR12
J112857.85+575909.84	20.89 ± 0.05	19.50 ± 0.03	19.20 ± 0.06	16.64 ± 0.08	15.84 ± 0.14	5.00	−27.16	DR12
J112956.09−014212.44	21.94 ± 0.11	19.58 ± 0.02	19.47 ± 0.07	15.11 ± 0.04	14.44 ± 0.05	4.87	−26.96	DR12
J113246.50+120901.70	21.25 ± 0.08	19.68 ± 0.04	19.21 ± 0.06	16.14 ± 0.07	15.37 ± 0.11	5.17	−27.41	DR7
J114657.79+403708.67	20.95 ± 0.05	19.38 ± 0.03	19.25 ± 0.05	16.03 ± 0.06	15.29 ± 0.09	4.98	−26.98	DR12
J120055.62+181733.01	21.25 ± 0.08	19.62 ± 0.03	19.44 ± 0.08	16.55 ± 0.08	15.77 ± 0.13	5.00	−26.82	DR12
J120441.73−002149.63	20.74 ± 0.04	19.21 ± 0.02	18.93 ± 0.04	15.94 ± 0.06	15.34 ± 0.11	5.09	−27.34	DR12
J120829.27+394339.72	20.79 ± 0.06	19.04 ± 0.02	19.06 ± 0.05	15.80 ± 0.05	15.09 ± 0.08	4.94	−27.25	Paper I
J120952.73+183147.21	21.57 ± 0.11	19.80 ± 0.04	19.44 ± 0.08	16.11 ± 0.06	15.38 ± 0.10	5.15	−27.00	DR12
J124942.12+334953.85 <sup>c</sup>	20.48 ± 0.04	19.14 ± 0.02	19.08 ± 0.05	16.23 ± 0.06	15.46 ± 0.09	4.93	−27.19	Schneider1991
J125353.35+104603.19	20.95 ± 0.04	19.37 ± 0.02	19.21 ± 0.05	15.33 ± 0.04	14.75 ± 0.07	4.91	−27.11	DR12
J131234.08+230716.36	20.74 ± 0.04	19.30 ± 0.02	18.97 ± 0.04	15.89 ± 0.05	15.28 ± 0.08	4.89	−27.22	DR12
J131814.03+341805.64	20.59 ± 0.03	19.05 ± 0.02	18.83 ± 0.04	15.20 ± 0.03	14.54 ± 0.05	4.82	−27.32	DR7
J133257.45+220835.91	21.12 ± 0.04	19.26 ± 0.02	19.23 ± 0.04	15.69 ± 0.05	14.89 ± 0.06	5.11	−27.39	Paper I
J134015.03+392630.70	21.19 ± 0.04	19.39 ± 0.02	19.19 ± 0.05	16.09 ± 0.05	15.48 ± 0.08	5.03	−27.17	DR12
J134040.24+281328.16	21.91 ± 0.10	20.02 ± 0.03	19.48 ± 0.08	16.13 ± 0.06	15.03 ± 0.07	5.34	−27.20	DR7
J134154.02+351005.71	21.32 ± 0.05	19.68 ± 0.02	19.45 ± 0.05	16.29 ± 0.06	15.64 ± 0.11	5.23	−26.95	DR12
J134408.62+152125.05	21.01 ± 0.06	19.40 ± 0.02	19.37 ± 0.06	16.20 ± 0.06	15.68 ± 0.13	4.87	−27.07	DR12
J134819.88+181925.82	20.80 ± 0.04	19.15 ± 0.02	19.18 ± 0.05	16.13 ± 0.06	15.57 ± 0.11	4.94	−27.10	DR12
J140404.65+031403.85	20.93 ± 0.06	19.52 ± 0.03	19.26 ± 0.07	16.09 ± 0.05	15.38 ± 0.09	4.90	−26.92	DR12
J141839.99+314244.07	21.54 ± 0.06	19.69 ± 0.03	19.27 ± 0.06	15.78 ± 0.04	15.11 ± 0.07	4.85	−26.92	DR12
J142325.92+130300.71	21.17 ± 0.05	19.67 ± 0.02	19.39 ± 0.08	15.98 ± 0.05	15.46 ± 0.09	5.02	−26.93	DR12
J142526.10+082718.46	20.54 ± 0.03	18.77 ± 0.02	18.92 ± 0.04	15.96 ± 0.04	15.41 ± 0.08	4.94	−27.13	DR12
J142634.33+204336.38	20.66 ± 0.03	19.13 ± 0.02	18.84 ± 0.04	15.59 ± 0.04	14.99 ± 0.06	4.82	−27.47	DR12



**Table 1**  
(Continued)

Name	$r_{\text{SDSS}}$	$i_{\text{SDSS}}$	$z_{\text{SDSS}}$	W1	W2	Redshift	$M_{1450}$	Notes <sup>a</sup>
J143605.00+213239.25	21.55 ± 0.07	19.95 ± 0.03	19.28 ± 0.06	16.42 ± 0.06	15.88 ± 0.11	5.22	−27.11	DR12
J143704.82+070807.72	20.62 ± 0.04	19.17 ± 0.02	19.16 ± 0.05	16.14 ± 0.06	15.62 ± 0.12	4.93	−27.10	Paper I
J143751.83+232313.35	21.19 ± 0.06	19.45 ± 0.02	19.16 ± 0.06	15.89 ± 0.04	14.97 ± 0.06	5.31	−27.29	DR12
J144350.67+362315.14	22.35 ± 0.14	20.15 ± 0.03	19.47 ± 0.06	15.90 ± 0.04	14.90 ± 0.05	5.12	−27.21	DR12
J152302.90+591633.05	21.39 ± 0.06	19.54 ± 0.02	19.22 ± 0.05	15.64 ± 0.03	15.13 ± 0.05	5.11	−27.40	Paper I
J153650.26+500810.33	20.18 ± 0.03	18.48 ± 0.02	18.51 ± 0.03	15.13 ± 0.03	14.52 ± 0.04	4.93	−27.70	DR12
J155657.36−172107.56	19.94 ± 0.04	18.43 ± 0.02	18.43 ± 0.05	15.09 ± 0.04	14.59 ± 0.06	4.75	−27.92	Paper I
J160111.17−182835.09	20.98 ± 0.15	19.37 ± 0.05	18.89 ± 0.09	15.65 ± 0.05	15.05 ± 0.08	5.06	−27.53	Paper I
J160734.23+160417.44	20.53 ± 0.03	19.15 ± 0.02	19.09 ± 0.06	16.09 ± 0.06	15.43 ± 0.09	4.76	−27.08	DR12
J161622.11+050127.71	20.16 ± 0.03	18.67 ± 0.02	18.59 ± 0.04	15.90 ± 0.06	15.17 ± 0.09	4.87	−27.80	DR7
J162045.64+520246.65	20.77 ± 0.04	18.97 ± 0.02	18.94 ± 0.04	15.30 ± 0.03	14.70 ± 0.04	4.79	−27.31	Paper I
J162315.28+470559.90	20.87 ± 0.05	19.52 ± 0.03	19.23 ± 0.07	15.57 ± 0.03	14.76 ± 0.05	5.13	−27.62	Paper I
J162623.38+484136.47	20.06 ± 0.02	18.50 ± 0.01	18.40 ± 0.03	15.51 ± 0.04	15.01 ± 0.05	4.84	−27.86	DR12
J162626.50+275132.50	21.47 ± 0.06	19.17 ± 0.02	18.53 ± 0.03	14.97 ± 0.03	14.21 ± 0.04	5.16	−27.95	DR12
J162838.84+063859.15	20.88 ± 0.04	19.56 ± 0.02	19.40 ± 0.05	16.68 ± 0.09	15.93 ± 0.17	4.85	−27.05	Paper I
J163810.39+150058.26	20.53 ± 0.04	18.83 ± 0.02	18.53 ± 0.04	15.10 ± 0.04	14.53 ± 0.05	4.76	−27.57	Paper I
J165354.62+405402.21	20.50 ± 0.03	18.59 ± 0.01	18.86 ± 0.05	15.42 ± 0.03	14.72 ± 0.05	4.96	−27.39	DR12
J165436.85+222733.80	19.74 ± 0.02	18.17 ± 0.01	18.08 ± 0.03	15.14 ± 0.04	14.58 ± 0.05	4.70	−27.99	DR12
J165635.46+454113.55	21.51 ± 0.06	19.70 ± 0.02	19.06 ± 0.04	16.22 ± 0.28	15.53 ± 0.07	5.34	−27.64	Paper I
J165902.12+270935.19	20.95 ± 0.07	19.34 ± 0.03	18.70 ± 0.04	15.92 ± 0.05	15.14 ± 0.07	5.31	−27.92	DR7
J173744.87+582829.66	20.79 ± 0.05	19.27 ± 0.02	19.15 ± 0.06	16.17 ± 0.05	15.56 ± 0.07	4.92	−27.30	DR7
J175114.57+595941.47	20.75 ± 0.04	19.09 ± 0.02	18.78 ± 0.04	15.66 ± 0.03	15.09 ± 0.05	4.83	−27.24	Paper I
J175244.10+503633.05	20.85 ± 0.04	18.82 ± 0.02	18.87 ± 0.05	15.13 ± 0.03	14.40 ± 0.03	5.02	−27.50	Paper I
J211105.62−015604.14	19.78 ± 0.02	18.11 ± 0.02	18.14 ± 0.03	15.02 ± 0.04	14.41 ± 0.05	4.85	−28.21	Paper I
J215216.10+104052.44	19.97 ± 0.03	18.36 ± 0.02	18.22 ± 0.03	14.67 ± 0.03	14.02 ± 0.04	4.79	−28.03	Paper I
J220008.67+001744.93	20.68 ± 0.04	19.09 ± 0.02	19.29 ± 0.06	16.20 ± 0.07	15.48 ± 0.13	4.77	−26.93	DR12
J220106.63+030207.71	20.58 ± 0.03	19.11 ± 0.02	18.90 ± 0.04	15.98 ± 0.06	15.20 ± 0.10	5.06	−27.59	Paper I
J220226.77+150952.38	20.28 ± 0.03	18.69 ± 0.02	18.47 ± 0.03	15.74 ± 0.05	15.20 ± 0.08	5.07	−28.02	Paper I
J222509.19−001406.82	20.46 ± 0.04	19.01 ± 0.03	18.71 ± 0.04	15.93 ± 0.05	15.41 ± 0.11	4.85	−27.37	DR12
J222514.38+033012.50	21.74 ± 0.14	20.02 ± 0.05	19.47 ± 0.10	16.50 ± 0.08	15.69 ± 0.13	5.24	−27.17	Paper I
J222612.41−061807.29	20.32 ± 0.04	18.76 ± 0.02	18.73 ± 0.05	15.64 ± 0.05	14.96 ± 0.09	5.08	−27.83	Paper I
J225257.46+204625.22	20.65 ± 0.04	19.16 ± 0.02	19.23 ± 0.06	16.27 ± 0.06	15.52 ± 0.10	4.91	−27.00	Paper I
J232939.30+300350.78	20.87 ± 0.05	19.37 ± 0.02	18.93 ± 0.04	16.21 ± 0.06	15.43 ± 0.10	5.24	−27.72	Paper I
J234241.13+434047.46	21.17 ± 0.06	19.26 ± 0.02	18.97 ± 0.05	15.57 ± 0.04	14.73 ± 0.06	4.99	−26.93	Paper I
J234433.50+165316.48	20.23 ± 0.03	18.46 ± 0.02	18.52 ± 0.03	15.22 ± 0.04	14.56 ± 0.06	5.00	−27.93	Paper I

**Notes.**

<sup>a</sup> Quasars from the SDSS DR7 and DR12 quasar catalogs are labeled as “DR7” and “DR12.” Quasars newly identified by us are labeled as “Paper I.” Two quasars from McGreer et al. (2009) and Schneider et al. (1991) were also spectroscopically observed by us and we use our new spectra to do the  $M_{1450}$  calculation. See the details for our newly observed quasars in Paper I. All  $M_{1450}$  values are corrected using our adopted cosmology.

<sup>b</sup> This quasar discovered by McGreer et al. (2009) using the radio-selection method was also observed by us and we use the new spectra for the  $M_{1450}$  calculation.

<sup>c</sup> This quasar discovered by Schneider et al. (1991) was also observed by us and we use the new spectra for the  $M_{1450}$  calculation.

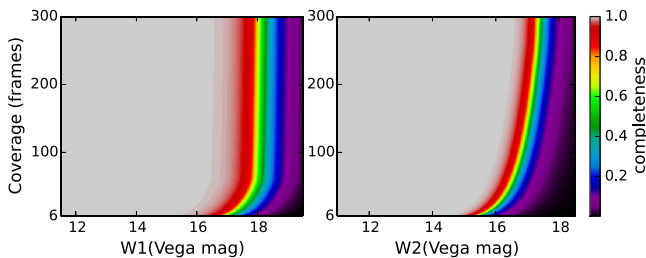


**Figure 2.** Empirical models of 2D detection completeness in ALLWISE W1 and W2 bands, which is from the Explanatory Supplement to the ALLWISE Data Release Products. Our sample limited with  $W1 < 17$  and  $\sigma_{W2} < 0.2$  will be effected slightly by the detection incompleteness at the faint end.

ALLWISE coverage also affects the photometric errors of detected sources. The photometric error in W1/W2 will be a function of magnitude and coverage. We used all point sources in our ALLWISE sources sample discussed above to model the empirical magnitude–coverage–magnitude error relations for

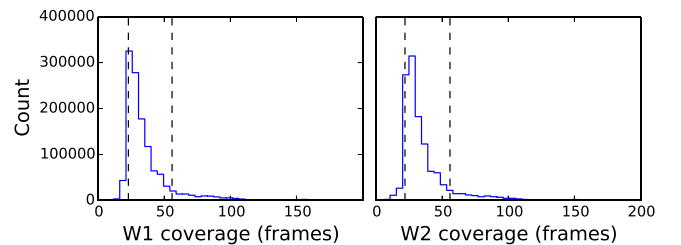


**Figure 3.** Distributions of W1/W2 frame coverages in the whole SDSS footprint. Dashed lines show the 10% and 90% tile ALLWISE coverage.

the ALLWISE W1 and W2 bands. The ALLWISE sensitivity improves approximately as the square root of the depth of coverage,  $\sigma \propto 1/\sqrt{N_{\text{cov}}}$ ,  $N_{\text{cov}}$  is the number of frame coverage. Considering this, we first eliminated the effect of coverage on magnitude errors and then fit the relations between W1/W2 magnitude and coverage-corrected magnitude error. Based on the *WISE* all-sky magnitude-error relation (Wright et al. 2010),

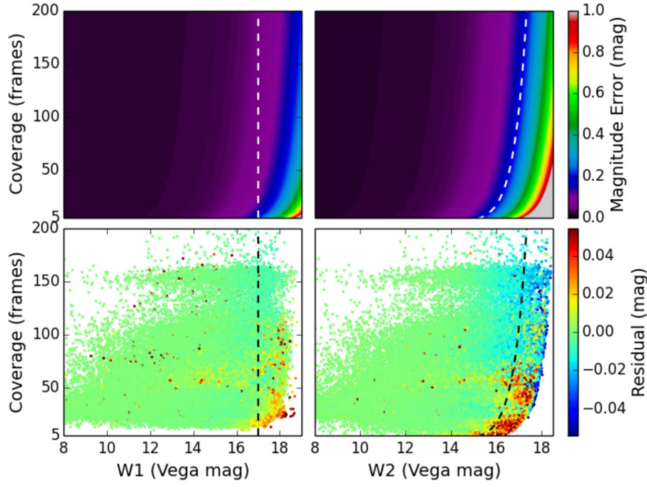


**Figure 4.** Top: the magnitude–coverage–magnitude error relations for the ALLWISE W1 and W2 bands. Bottom: the residuals of magnitude error, observed data minus model fitted. The dashed lines denote our W1 and W2 magnitude limit ( $W1 < 17$ ,  $\sigma_{W2} < 0.2$ ). Our model reproduced the ALLWISE photometric errors in SDSS footprint well.

the final ALLWISE magnitude–coverage–error relation we obtained is

$$\sigma(m, N_{\text{cov}}) = a + [2.5/\ln(10)]n/10^{-0.4m}/\sqrt{N_{\text{cov}}} . \quad (5)$$

Where  $m$  is the magnitude in W1/W2. Constant  $a$  is basic photometric error, equal to 0.01 in WLSE all-sky photometry (Wright et al. 2010). We found that  $a$  should be 0.022 for W1 and 0.019 for W2 in ALLWISE photometry. The best-fitted parameter  $n$  is  $6.43\text{e}-8$  for W1,  $2.71\text{e}-7$  for W2. Figure 4 shows our empirical model compared with observed data.

### 3.2. Selection Function of Color–Color Selection

To estimate the completeness of our selection criteria, we generate a sample of simulated quasars following the procedure in Fan (1999). M13 updated the spectral model of Fan (1999) and applied it to higher redshift, assuming that the quasar spectral energy distributions do not evolve with redshift (Kuhn et al. 2001; Yip et al. 2004; Jiang et al. 2006). We extend this model toward redder wavelengths to cover the ALLWISE W1, W2 bands for quasars at  $z = 4-6$  (I. D. McGreer et al. 2016, in preparation). The quasar spectrum from M13 is modeled as a power-law continuum with a break at 1100 Å. For redder wavelength coverage, we added three new breaks at 5700, 10850, and 22300 Å. The slope ( $\alpha_\nu$ ) from 5700 to 10850 Å follows a Gaussian distribution of  $\mu(\alpha) = -0.48$  and  $\sigma(\alpha) = 0.3$ ; the middle range has a slope with the distribution of  $\mu(\alpha) = -1.74$  and  $\sigma(\alpha) = 0.3$ ; and at the red end, the slope distribution has  $\mu(\alpha) = -1.17$  and  $\sigma(\alpha) = 0.3$  (Glikman et al. 2006). The parameters of emission lines are derived from the composite quasar spectra (Glikman et al. 2006). Although the composite spectrum from Glikman et al. (2006) is constructed from fainter lower redshift quasars, it does not have obvious difference with composite spectra built from luminous quasars at high redshift (e.g., Selsing et al. 2016). It is the only one we know that can cover both W1 and W2 bands in the redshift range of our simulation ( $4 < z < 6$ ). The IGM absorption model is the same as M13, which extends the  $\text{Ly}_\alpha$  forest model based on the work of Worseck & Prochaska (2011) to higher redshift by using the observed number

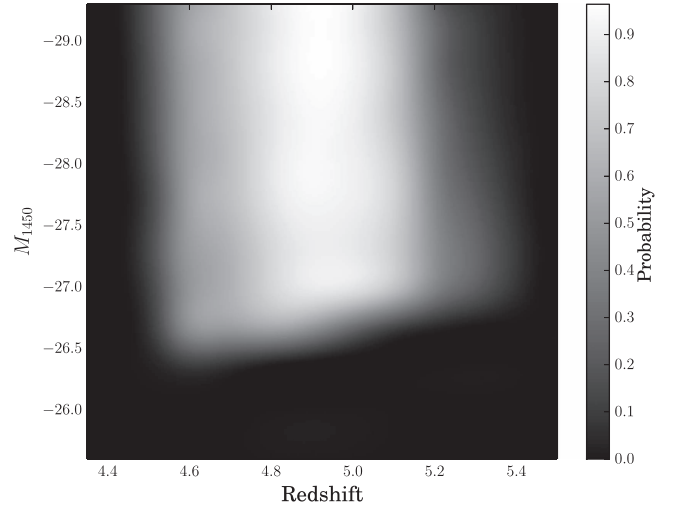


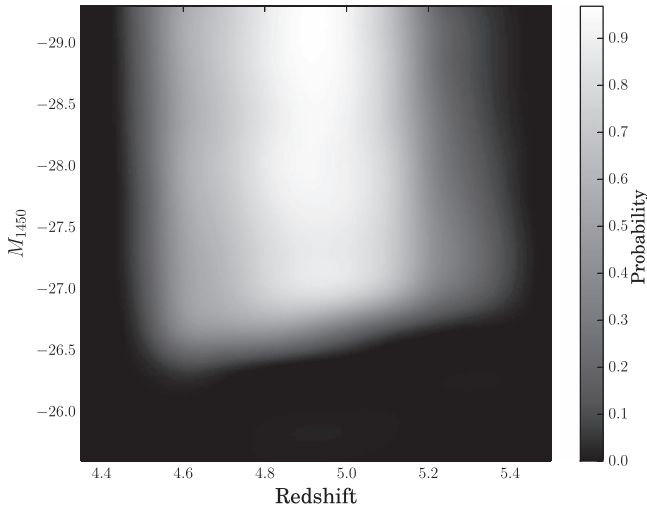
**Figure 5.** Selection function of our survey ( $z_{\text{SDSS}} < 19.5$ ) based on position-dependent ALLWISE coverage. The probability is the fraction of simulated quasars, which can be selected by our selection criteria in each  $(M_{1450}, z)$  bin.

densities of high column density systems (Songaila & Cowie 2010). Compared to M13, we have made minor modifications for Fe emission. We use the template from Vestergaard & Wilkes (2001) for wavelengths shorter than 2200 Å. For 2200–3500 Å, we use the template from Tsuzuki et al. (2006), which separates the Fe II emission from the Mg II  $\lambda 2798$  line. A template from Boroson & Green (1992) covering 3500–7500 Å is also added.

Based on this model, we generate a sample of simulated quasars and then calculate the selection function of our color–color selection. We construct a grid of quasars in the redshift range of  $4 < z < 6$  and the luminosity range of  $-29.5 < M_{1450} < -25.5$ . A total of 314,000 simulated quasars has been generated and evenly distributed in the  $(M_{1450}, z)$  space. There are  $\sim 200$  quasars in each  $(M_{1450}, z)$  bin with  $\Delta M = 0.1$  and  $\Delta z = 0.05$ . We assign optical photometric errors, which are from the SDSS main survey, and photometric uncertainties of the W1 and W2 bands using the empirical magnitude–coverage–error relations discussed above. We added the ALLWISE detection completeness into the selection probability calculation.

We calculate the ALLWISE detection probability by randomly choosing a unique sky position from our 1,220,000 positions for each simulated quasar, and thus obtained an ALLWISE detection probability of each simulated quasar based on its frame’s coverage and W1 and W2 magnitude. For each  $(M_{1450}, z)$  bin ( $\Delta M = 0.1$  and  $\Delta z = 0.05$ ) discussed above, we obtain a mean detection probability. Then we calculate the fraction of simulated quasars selected by our selection criteria in each  $(M_{1450}, z)$  bin as the selection probability, shown in Figure 5.

As shown in Figure 5, after relaxing the traditional  $r - i / i - z$  color cut and adding the  $W1 - W2$  color, our color selection criteria show a high completeness at  $4.8 < z < 5.2$  and extend the selection region to  $z \sim 5.4$ . Within the central bright region ( $4.8 < z < 5.2$  and  $M_{1450} < -26.8$ ), the mean completeness reaches 78%. Extended to the range of  $4.7 < z < 5.4$ , the mean completeness is  $\sim 60\%$ . At a redshift lower than 4.5 or higher than 5.4, the completeness is below 5%. At  $z < 4.7$ , the  $W1 - W2$  color becomes bluer; our  $W1 - W2 > 0.5$  cut will miss some quasars at  $z < 4.7$  (see



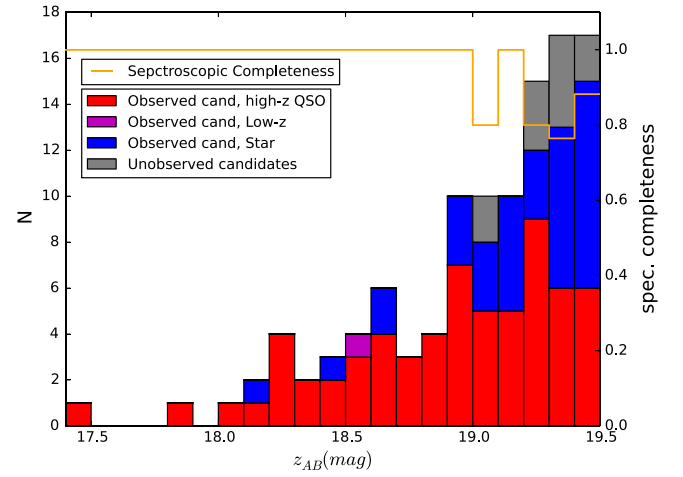
**Figure 6.** Selection function of our survey ( $z_{\text{SDSS}} < 19.5$ ) using 10% tile ALLWISE coverage,  $N_{\text{cov}} = 23$  for W1,  $N_{\text{cov}} = 22$  for W2. Comparing with Figure 5, the change of probability is small.

Figure 3 in Paper I). However, the exact completeness is more sensitive to the assumption we made about the rest-frame optical continuum of high-redshift quasars at  $4.5 < z < 4.7$  due to the fast change of W1 – W2 color here. The uncertainty of the simulation in this redshift range is higher than that at  $z > 4.7$ . Therefore, we restrict our quasar sample for the QLF calculation to  $z \geq 4.7$ . At  $5.2 < z < 5.4$ , although the completeness becomes lower, our selection has explored a higher redshift range with higher completeness than previous works at  $z \sim 5$ . Thus, we limit our sample with  $z < 5.4$ .

To see how the ALLWISE coverage affects our selection function, we also calculate the selection function by assuming a fixed number of coverage, 10% tile ALLWISE coverage ( $N_{\text{cov}} = 23$  for W1,  $N_{\text{cov}} = 22$  for W2), shown in Figure 6. The difference in the selection function between using 10% tile coverage and position-dependent coverage is less than 5% at  $M_{1450} < -27$  and increases to  $\sim 10\%$  at  $M_{1450} < -26.8$ , to 15%–20% at a fainter range. We also compare the QLF result base on 10% tile coverage and position-dependent coverage. The change of the parameters of best-fitted QLFs is  $\sim 0.05$ , much smaller than error bars. We use the position-dependent coverage selection function to calculate the parametric QLF. When we calculate the selection probability of each quasar in our sample for a binned QLF measurement, we use the real ALLWISE coverage to calculate the ALLWISE detection completeness of each quasar. The agreement between binned QLF and best-fit parametric QLF (See Sections 4.1 and 4.2) shows that our ALLWISE coverage model and the selection function using mean detection incompleteness are reasonable.

### 3.3. Spectroscopic Incompleteness

We spectroscopically observed 99 out of 110 candidates. The spectroscopic completeness reaches 100% at  $z_{\text{SDSS}} \leq 19$ ; at the fainter end, the completeness is lower but it still has a high value around 80%. The histogram of our observed and unobserved candidates is shown in Figure 7. The completeness is a function of  $z$ -band magnitude. We use this function to correct the incompleteness from spectral coverage, assuming the probability of an unobserved candidate to be a quasar is the same as in the observed sample. As shown, the quasar fraction



**Figure 7.** Spectroscopic incompleteness of our 110  $z \sim 5$  quasar candidates. The orange line denotes the spectroscopic incompleteness as a function of  $z$ -band magnitude. The histogram is divided into several components filled by different colors and represents newly identified high-redshift quasars (red), low-redshift quasars (purple), stars (blue), and unobserved candidates (gray).

**Table 2**  
Binned QLF

$M_{1450}$	$N$	$N_{\text{cor}}$	$\log \Phi$	$\Delta \Phi^a$
$-28.99^b$	1	18.2	$-9.48$	0.33
$-28.55$	4	7.7	$-9.86$	0.08
$-28.05$	14	24.4	$-9.36$	0.15
$-27.55$	26	44.4	$-9.09$	0.19
$-27.05$	54	103.1	$-8.70$	0.32

**Notes.**

<sup>a</sup>  $\Delta \Phi$  is in units of  $10^{-9} \text{ Mpc}^{-3} \text{ mag}^{-1}$ .

<sup>b</sup> Within the brightest magnitude bin, there is only one quasar. Therefore, we use its  $M_{1450}$  as the  $M_{1450}$  of this bin.

in our unknown candidate sample becomes lower at the faint end. That is caused by the fact that there are more known quasars at  $z_{\text{SDSS}} > 19$ , and these known quasars are not plotted in this figure.

## 4. A NEW DETERMINATION OF THE QLF AT $Z \sim 5$

### 4.1. Binned QLF

To compute the binned QLF, we divide our sample into several bins. Due to the narrow redshift interval of our sample, we only use one redshift bin and do not include any evolution with redshift. We then divide our sample into 5 mag bins with  $\Delta M_{1450} = 0.5 \text{ mag}$  over the magnitude range  $-26.8 < M_{1450} < -29.3$  (see Figure 1). We calculate the binned luminosity function by using the Page & Carrera (2000) modification of the  $1/V_a$  method (Schmidt 1968; Avni & Bahcall 1980) for flux limit correction. The final selection function is applied after all incompleteness corrections have been applied for each quasar. The result for the binned QLF and number counts are listed in Table 2. In the table, the number counts and corrected number counts derived by applying all incompleteness corrections are denoted as  $N$  and  $N_{\text{cor}}$  respectively. The result is also displayed in Figure 8 as red squares together with the binned QLF data from the SDSS main (black) and Stripe 82 (blue) samples in M13 for comparison. Data from M13 have been corrected to  $z = 5.05$  by using the quasar redshift evolution at high

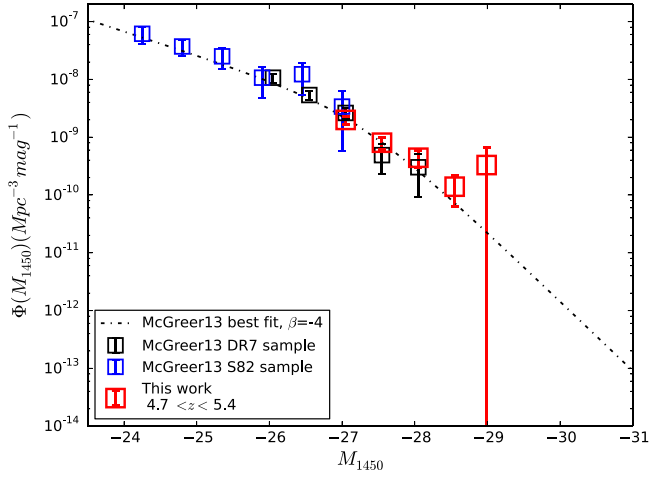


**Figure 8.** Binned QLF at  $z = 5.05$  ( $4.7 \leq z < 5.4$ ). The red squares represent our binned QLF data. The blue and black squares denote the binned QLF data from the Stripe 82 sample and the SDSS main sample in M13. These data have been corrected to  $z = 5.05$  by using the redshift evolution proposed by Fan et al. (2001b). The black dashed-dotted line shows the best fitting QLF from M13 with the bright end slope  $\beta = -4$ .

redshifts according to Fan et al. (2001b). Compared to previous results, our binned QLF has more luminous quasars and extends the measurement of the  $z \sim 5$  QLF to  $M_{1450} = -29$ , and thus gives a smaller error bar in each bin at  $M_{1450} < -27.05$ . Our data show a similar result, but suggest a higher value at the bright end. The binned QLF in the brightest bin has a large error bar due to the fact that there is only one quasar in this bin.

#### 4.2. Maximum Likelihood Fitting

The binned QLF result, while non-parametric, is dependent on the choice of binning. Here we derive a parametric QLF by performing a maximum likelihood fit for each quasar in the sample. We model the QLF using the most common double power-law form (Boyle et al. 2000):

$$\Phi(M, z) = \frac{\Phi^*(z)}{10^{0.4(\alpha+1)(M-M^*)} + 10^{0.4(\beta+1)(M-M^*)}}, \quad (6)$$

where  $\alpha$  and  $\beta$  are the faint end and the bright end slopes,  $M^*$  is the break magnitude, and  $\Phi^*(z)$  is the normalization. These four parameters have been suggested to evolve with redshift. Following previous work, we adopt the rapid decline in quasar number density at high redshift from Fan et al. (2001b) as the QLF evolution within our narrow redshift interval,  $\Phi^*(z) = \Phi^*(z=6) \times 10^{k(z-6)}$ , where  $k = -0.47$  (Fan et al. 2001b).<sup>11</sup> Here we also normalize  $\Phi^*$  to  $z = 6$  for easier comparison to the higher redshift results.

Due to the fact that our quasar sample covers the magnitude range of  $M_{1450} \leq -26.8$ , and the break magnitude given by M13 is around  $-26$  to  $-27$ , our sample cannot be used to constrain the faint end slope. For measurement of the break magnitude  $M^*$ , we combine our luminous quasar sample with the S82 and DR7 quasar samples from M13 and then carry out

<sup>11</sup> To see how the results depend on  $\Phi^*(z)$  evolution, we varied the value of  $k$  from  $-0.3$  to  $-0.7$ . We find that the form of  $\Phi^*(z)$  evolution has little effect on the other parameters when doing the fits. The changes are within  $1\sigma$ . Furthermore, due to the narrow redshift range we used, the  $\log(\Phi^*(z))$  is also affected only slightly by varying the form of the evolution.

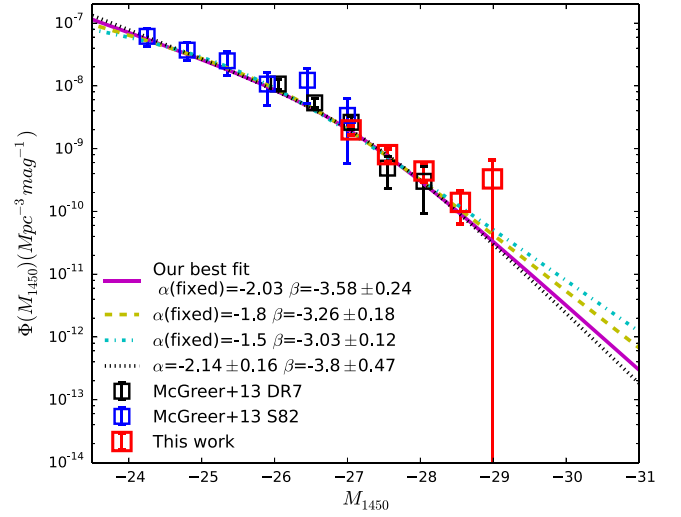


**Figure 9.** Double power-law fits using maximum likelihood fitting compared with the binned QLF data from the S82 sample, the DR7 sample, and our luminous quasar sample. The results based on fixed  $\alpha$  and on four free parameters are plotted for comparison. We fix the faint-end slope  $\alpha$  at  $-2.03$  (purple line),  $-1.8$  (yellow dashed line), and  $-1.5$  (cyan dotted-dashed line) and do the fits respectively. Then we also allow all four parameters to be free (Green dashed line). When we change the faint-end slope  $\alpha$  from  $-2.03$  to  $-1.8$  and  $-1.5$ , the bright end slope  $\beta$  is flattened, but it only changes a little. The break magnitude becomes fainter following the change of  $\beta$ . When we allow all four parameters to be free, we get a steeper bright end slope  $\beta = -3.80$ .

parametric fits for the QLF for all observed quasars in the combined sample. The DR7 sample has a large number of overlaps with our luminous quasar sample. Therefore, we select DR7 quasars only in the magnitude range  $-26.8 < M_{1450} < -25.8$  to construct the combined sample. For the S82 and DR7 samples, we use the same incompleteness corrections as in M13. We use maximum likelihood estimation to derive the fit. The maximum likelihood fit (Marshall et al. 1983) for a luminosity function aims to minimize the log likelihood function  $S$ , which is equal to  $-2 \ln L$ , where  $L$  is the likelihood function:

$$S = -2 \sum_i^N \ln[\Phi(M_i, z_i)] + 2 \iint \Phi(M, z) p(M, z) \frac{dV}{dz} dM dz, \quad (7)$$

where the first term is the sum over all observed quasars in the sample, and the second term is integrated over the full range of absolute magnitude and redshift of the sample (Marshall et al. 1983; Fan et al. 2001a);  $p(M, z)$  is the probability for a quasar to be observed by the survey at given absolute magnitude  $M_{1450}$  and redshift  $z$ . It includes all incompleteness corrections discussed above. The second term represents the total number of expected quasars in the survey with a given luminosity function, and provides the normalization for the likelihood function. The confidence intervals are determined from the likelihood function by assuming a  $\chi^2$  distribution of  $\Delta S$  ( $=S - S_{\min}$ ) (Lampton et al. 1976).

We first fix the faint-end slope  $\alpha$  to be  $-2.03$ , as given by M13. We find the luminosity function parameters to be  $\log \Phi^*(z=6) = -8.82 \pm 0.15$ ,  $M_{1450}^* = -26.98 \pm 0.23$  and  $\beta = -3.58 \pm 0.24$ . This result is plotted in Figure 9 and shows excellent agreement with our binned QLF. In order to



**Table 3**  
Parameters of Fits

$\alpha$	$\beta$	$M_{1450}^*$	$\log \Phi^*(z = 6)$
-2.03	$-3.58 \pm 0.24$	$-26.98 \pm 0.23$	$-8.82 \pm 0.15$
-1.80	$-3.26 \pm 0.18$	$-26.28 \pm 0.29$	$-8.35 \pm 0.17$
-1.50	$-3.03 \pm 0.12$	$-25.56 \pm 0.29$	$-7.94 \pm 0.15$
$-2.14 \pm 0.16$	$-3.80 \pm 0.47$	$-27.32 \pm 0.53$	$-9.07 \pm 0.40$

**Note.** We fix the faint slope  $\alpha$  to be  $-2.03$ ,  $-1.8$ , and  $-1.5$  respectively. Then we allow all four parameters to be free.  $\alpha = -2.03$  is measured from the combination of the SDSS S82 and DR7 samples in M13. We adopt the result with fixed  $\alpha = -2.03$  as our best fit.

investigate how the different values of  $\alpha$  affect our result, we also assume the faint-end slope  $\alpha$  to be  $-1.8$ , similar to what was measured from quasar samples at  $z \geq 4$  (Glikman et al. 2010; Willott et al. 2010; Masters et al. 2012; McGreer et al. 2013), and to  $-1.5$ , typical for lower redshift measurements at  $z \lesssim 3$  (Croom et al. 2009). The values of parameters assuming different faint-end slopes are listed in Table 3. When we change the faint-end slope  $\alpha$  from  $-2.03$  to  $-1.8$  and  $-1.5$ , the bright end slope  $\beta$  is flattened but only at the  $\lesssim 1\sigma$  level. The break magnitude becomes fainter more significantly following the change of  $\beta$ . If we allow all four parameters to be unconstrained, we derive a steeper bright end slope  $\beta = -3.80$  and a very bright break magnitude of  $M_{1450}^* = -27.33$  with significantly larger error bars. Allowing all parameters to be free has many degeneracies, which is why the uncertainty ranges are larger. In this case, the faint-end slope  $\alpha$  also becomes steeper ( $\alpha = -2.15$ ). We need more data to better constrain a four-parameter fit, especially for  $M_{1450} < -28.3$ . Considering that  $\alpha = -2.03$  derived by M13 is a strong constraint on the faint-end slope, we adopt the result based on fixed  $\alpha = -2.03$  as our best fit. The fitted QLFs for different cases are plotted in Figure 9.

We calculate the confidence regions to investigate the degeneracy between the bright end slope and break magnitude; the results are shown in Figure 10. The regions filled with different colors illustrate  $1\sigma$  (68.3%),  $2\sigma$  (95.4%), and  $3\sigma$  (99.7%) regions, respectively. We generate the probability contours by calculating  $S_{\min}$  for each  $(M_{1450}, \beta)$  point and allowing  $\log \Phi(z = 6)^*$  to be free at each point with the fixed  $\alpha = -2.03$ . Figure 10 shows that our data constrain  $\beta$  to the range of  $-4.83 < \beta < -2.78$  at 95% confidence; this is flatter than the result from M13, which shows  $\beta < -3.1$  at 95% confidence, although the best fit from M13,  $\beta = -4$ , lies within our  $2\sigma$  region.

We compare the parameters of our result with previous work at different redshifts to study the evolution of the QLF. In Figure 11, we plot the evolution of the normalization  $\Phi^*$ , the break magnitude  $M_{1450}^*$ , and the bright end slope  $\beta$  with redshift. Ross et al. (2013) measured the QLF at  $2.2 < z < 3.5$  using the BOSS DR9 quasar sample and concluded that the QLF can be described well by an LEDE model at this redshift range. In this model, the evolutions of normalization and break luminosity with redshift are expressed in a log-linear relation, and slopes of the double power law are fixed. M13 add a point at  $z = 4.9$  and combine the result from Masters et al. (2012) at  $z = 4$  and the result from Willott et al. (2010) at  $z = 6$  to modify this model. They found that the slope of the normalization evolution was steeper ( $c_1 = -0.7$ ) and the slope of the break magnitude evolution was shallower ( $c_2 = -0.55$ ). Now

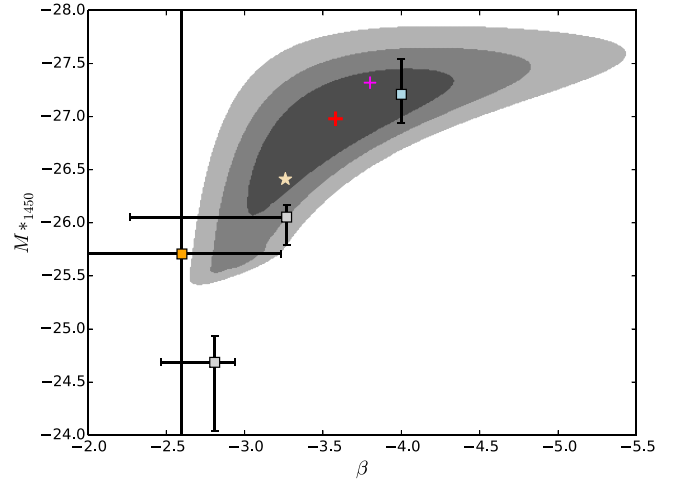


**Figure 10.** Confidence region for  $\beta$  and  $M_{1450}^*$ . The regions filled with different shades of gray denote  $1\sigma$  (68.3%),  $2\sigma$  (95.4%), and  $3\sigma$  (99.7%) regions, respectively. For comparison, we plot our best-fit result (red cross) and the result of the four-parameter fit (magenta cross) together with the best fit from other work. The light blue square denotes the best fit from M13 at  $z \sim 5$ . The white star shows the result from Willott et al. (2010) for fixed  $\alpha = -1.8$  (uncertainties of the fit were not reported) at  $z \sim 6$ . The yellow square represents the best fit from Masters et al. (2012), which used the faint quasar sample in the COSMOS field in conjunction with the bright quasar sample from Richards et al. (2006) to model a double power-law QLF at  $z \sim 4$ . We also plot the points (gray squares) to show the best fits for binned data in the  $z = 2.2$  (left) and  $3.4$  (right) redshift bins from the BOSS S82 sample (Ross et al. 2013). All data have been corrected to our adopted cosmology.

we add our new measurement at  $z = 5.05$  and the point at  $z = 6$  from Kashikawa et al. (2015) in case 1. The result from Kashikawa et al. (2015) includes the discovery of new faint  $z \sim 6$  quasars and places stronger constraints on the faint-end slope and break magnitude of the  $z \sim 6$  QLF. Then we use all of these points to fit the LEDE model.

$$\log [\Phi^*(z)] = \log [\Phi^*(z = 2.2)] + c_1(z - 2.2), \quad (8)$$

$$M_{i,2}^*(z) = M_{i,2}^*(z = 2.2) + c_2(z - 2.2), \quad (9)$$

where  $M_{i,2} \equiv M_i(z = 2) = M_{1450} - 1.486$  is the absolute  $i$ -band magnitude at  $z = 2$  (Richards et al. 2006), corresponding to rest-frame  $\sim 2600 \text{ \AA}$  in the assumption of a spectral index of  $\alpha_\nu = -0.5$ . We obtain values of  $\log \Phi^*(z = 2.2) = -5.87 \pm 0.07$  and  $c_1 = -0.81 \pm 0.03$ ;  $M_{i,2}^*(z = 2.2) = -26.68 \pm 0.15$  and  $c_2 = -0.50 \pm 0.08$ . Note that the errors of parameters are standard deviation errors of fit. We only use these points without uncertainties to do the fit because the uncertainties of the best fit in Willott et al. (2010) are not reported. The real errors should be larger than the fitting errors explored here. Our result is consistent with the LEDE model but prefers a steeper slope of  $\log \Phi^*(z)$  evolution and a flatter slope of the break magnitude evolution.<sup>12</sup>

<sup>12</sup> Our results can also be compared to Figure 19 of M13; however, the BOSS data used in M13 were based on a pre-publication analysis of the DR9 sample, and were later updated in Ross et al. (2013). Here we use the final version of the BOSS data from that work.

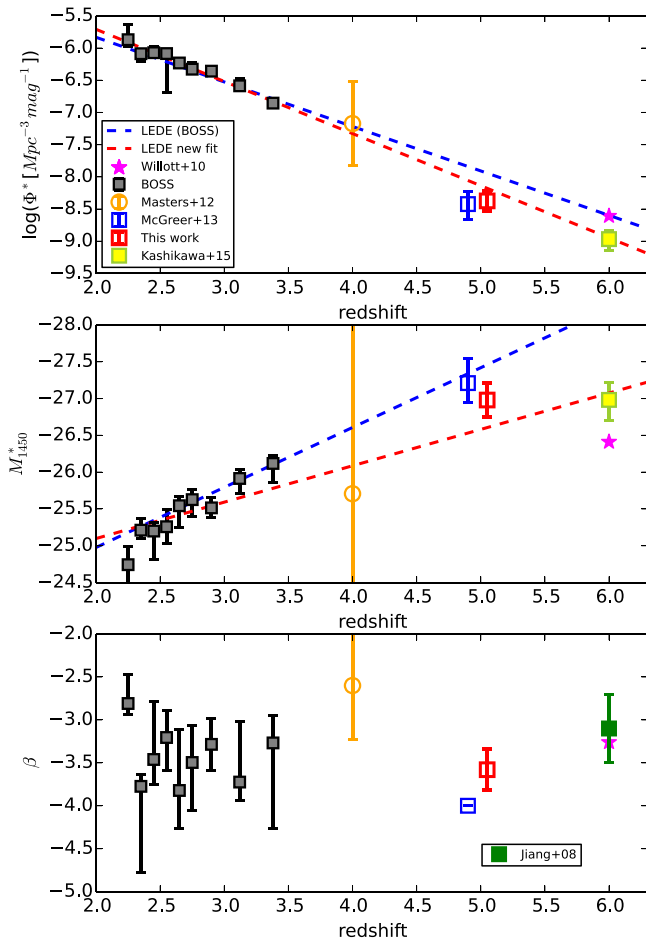


**Figure 11.** Evolution of QLF parameters: normalization  $\Phi^*$  (upper), break magnitude  $M_{1450}^*$  (middle), and the bright end slope  $\beta$  (bottom). We compare our best-fit QLF parameters with previous results at similar and different redshifts to show the evolution of parameters from redshift of  $z \sim 2$  to 6. The gray squares at  $2.2 < z < 3.5$  are the best fits for each redshift bin from the BOSS DR9 QLF, which were measured by using a sample of  $\sim 6000$  variability-selected quasars in Stripe 82 (Ross et al. 2013). The orange circle is the best fit from Masters et al. (2012) at  $z = 4$ . The blue square represents the best fit from M13 at  $z = 4.9$ , and our best fit at  $z = 5.05$  is plotted as a red square. At  $z = 6$ , in the  $\Phi^*$  and  $M_{1450}^*$  plots, we plot the result from Willott et al. (2010) with  $\alpha = -1.8$  (magenta star) and Kashikawa et al. (2015) in their case 1 fits (yellow square). In the  $\beta$  – redshift plot, we plot the result from Willott et al. (2010) and the single power-law fit of Jiang et al. (2008) at  $z = 6$  because Kashikawa et al. (2015) fit their data with a fixed bright end slope. The blue dashed lines in the  $\Phi^*$  and  $M_{1450}^*$  plots represent the LEDE model from Ross et al. (2013). The red dashed lines are our new fits. All data have been corrected to our adopted cosmology.

## 5. DISCUSSION

### 5.1. Contribution to the Ionizing Background

Previous measurements of the QLF at  $z = 5$  and 6 have shown evidence that quasars cannot produce the entire required ionizing photon background (M13; Meiksin 2005; Bolton & Haehnelt 2007; Willott et al. 2010; Kashikawa et al. 2015) at those redshifts. It is suggested that quasars can contribute  $\sim 30\%$ – $70\%$  of the ionizing photons required to maintain full ionization at  $z = 5$  (M13), and produce about several percent to 15% at  $z = 6$  (Willott et al. 2010; Kashikawa et al. 2015), depending on the assumed IGM clumping factor  $C$ . Here we update the quasar contribution to the high-redshift ionizing background using our new QLF at  $z \sim 5$ .

We calculate the comoving emissivity of quasars at the Lyman limit by  $\epsilon(z) = \int \phi(L_\nu, z) L_\nu dL_\nu \text{ erg s}^{-1} \text{ Hz}^{-1} \text{ Mpc}^{-3}$ , assuming the escape fraction of ionizing radiation from quasars  $f = 1$ . We integrate our parametric QLF  $\Phi(M_{1450}, z)$  and then convert it into emissivity at  $\lambda = 912 \text{ \AA}$ . For the conversion, we adopt the UV slopes from Stevans et al. (2014), who suggest a gradual break wavelength at  $1000 \text{ \AA}$ , with the index  $\alpha_\nu = -1.41$  in the extreme ultraviolet and a spectral index  $\alpha_\nu = -0.83$  at wavelengths above the break. By integrating our best-fit QLF to  $M_{1450} = -20$ , we derive an ionizing photon density  $\dot{N}_Q = 6.06 \times 10^{49} \text{ Mpc}^{-3} \text{ s}^{-1}$ . When we use the QLF result with a fixed faint-end slope of  $\alpha = -1.8$ , the photon number density changes to  $\dot{N}_Q = 4.73 \times 10^{49} \text{ Mpc}^{-3} \text{ s}^{-1}$ . Using the QLF generated from the four-parameter fit, we get  $\dot{N}_Q = 7.37 \times 10^{49} \text{ Mpc}^{-3} \text{ s}^{-1}$ . The change of ionizing photon density is dominated by the change of the break magnitude  $M_{1450}^*$  and the faint-end slope  $\alpha$ . Luminous quasars make little contribution to the ionizing background, so a survey of faint quasars is required to give a more accurate measurement.

The required number of photons to balance hydrogen recombination and maintain full ionization was estimated by Madau et al. (1999) as a function of redshift. The number of required photons at  $z = 5$  is  $\dot{N}_{\text{ion}} = 3.38 \times 10^{50} (C/5) \text{ Mpc}^{-3} \text{ s}^{-1}$  in our adopted cosmology. The clumping factor  $C$  is crucial to estimate the contribution of quasars to the ionizing background. Madau et al. (1999) considered a recombination-dominated IGM and suggested a high value for the clumping factor  $C = 30$ . Recent work provides a lower clumping factor  $C < 10$ . Meiksin (2005) suggests that  $C \approx 5$  and a  $C \approx 2$ – $3$  at  $z = 6$  is suggested by some reionization models (McQuinn et al. 2011; Finlator et al. 2012; Shull et al. 2012). For  $C = 2$ , based on the result from our best-fit QLF, quasars are estimated to provide  $\sim 45\%$  of the required photons; while for  $C = 5$ , the fraction changes to 18%. This result agrees with previous work, suggesting that quasars may play some role in maintaining ionization at  $z \sim 5$  but have low possibilities of being the dominant source of ionizing photons (M13).

### 5.2. Radio-loud Fraction

Traditionally, quasars have been divided into two populations, radio-loud and radio-quiet (Kellermann et al. 1989). The similarity and difference between the evolution of radio-loud and radio-quiet quasars are thought to be related to black-hole mass, accretion, and spin. (Rees et al. 1982; Wilson & Colbert 1995; Laor 2000). The radio-loud fraction (RLF) has been suggested to evolve with optical luminosity and redshift by some work (e.g., Padovani 1993; La Franca et al. 1994; Hooper et al. 1995; Jiang et al. 2007; Kratzer & Richards 2015). In contrast to this, no evolution of the RLF is also found (e.g., Goldschmidt et al. 1999; Stern et al. 2000; Ivezić et al. 2002; Cirasuolo et al. 2003). Our luminous quasar sample is selected only by optical and near-infrared colors and thus it can be considered to be an unbiased sample for the study of the RLF.

We cross-match all 99 quasars in our sample with catalogs from Faint Images of the Radio Sky at Twenty-cm (FIRST; Becker et al. 1995) and the NRAO VLA Sky Survey (NVSS; Condon et al. 1998) and find 8 quasars with radio detections. We use  $3''$  matching radius for FIRST data, and  $5''$  for NVSS due to the lower resolution of NVSS. We calculate the radio loudness for these 8 quasars by assuming an optical spectral

**Table 4**  
Radio Detection and Radio Loudness

Name	$z$	$m_{1450}$	$f_{1.4 \text{ GHz, FIRST}}^a$	$f_{\text{err}, F}$	$f_{1.4 \text{ GHz, NVSS}}$	$f_{\text{err}, N}$	$f_{\nu, 2500}$	$f_{\nu, 4400}$	$f_{\nu, 5 \text{ GHz}}$	$R_{2500}$	$R_{4400}$	$M_{2500}^b$
J0011+1446	4.96	18.03	23.96	0.146	35.8	1.5	0.0491	0.0651	5.1933	105.8	79.7	-28.65
J0131-0321	5.18	18.09	32.83	0.123	31.4	1.0	0.0448	0.0594	6.9880	156.0	117.6	-28.66
J0741+2520	5.21	18.22	2.07	0.141	...	...	0.0396	0.0525	0.4395	11.1	8.4	-28.54
J0813+3508	4.92	19.17	20.04	0.156	35.6	1.1	0.0173	0.0229	4.3583	252.0	189.9	-27.50
J1146+4037	4.98	19.48	12.45	0.146	12.5	0.5	0.0129	0.0171	2.6940	209.3	157.8	-27.21
J1318+3418	4.82	19.09	3.73	0.148	3.5	0.4	0.0189	0.0251	0.8181	43.2	32.6	-27.54
J2329+3003 <sup>c</sup>	5.24	18.83	...	...	4.9	0.4	0.0224	0.0298	1.0380	46.2	34.9	-27.94
J2344+1653	5.00	18.54	...	...	15.3	0.6	0.0305	0.0404	3.3052	108.4	81.7	-28.15

**Notes.**

<sup>a</sup> Flux density and flux density error are in units of mJy.

<sup>b</sup> Data in this table are calculated based on cosmology  $H_0 = 70 \text{ km s}^{-1} \text{ Mpc}^{-1}$ ,  $\Omega_m = 0.3$ , and  $\Omega_\Lambda = 0.7$ .

<sup>c</sup> The two objects only detected by NVSS without FIRST detection are not covered by the FIRST footprint.

index of  $-0.5$  and radio spectral index of  $-0.5$  ( $f_\nu \propto \nu^\alpha$ ) and list them in Table 4. To compare with previous work at higher redshifts (Bañados et al. 2015), we adopt the radio/optical flux density ratio  $R_{4400} = f_{\nu, 5 \text{ GHz}}/f_{\nu, 4400 \text{ Å}}$  (Kellermann et al. 1989) and the criterion  $R > 10$  for the definition of a radio loud quasar, where  $f_{\nu, 5 \text{ GHz}}$  is the radio flux density at rest-frame 5 GHz, and  $f_{\nu, 4400 \text{ Å}}$  is the optical flux density at rest-frame 4400 Å. There are 7 quasars considered to be radio loud quasars among the 99 quasars. Therefore, we find a radio loud fraction  $\text{RLF} \sim 7.1\%$ . Considering FIRST with its 1 mJy flux limit and NVSS with its 2.5 mJy flux limit are not deep enough to detect all radio loud quasars, especially for quasars at  $z_{\text{SDSS}} > 19$ , 7.1% is a lower limit. This result shows agreement with the result from Bañados et al. (2015), which constrains the RLF at  $z \sim 6$  to be  $8.1_{-3.2}^{+5.0}\%$ . We also do the calculation using a radio spectral index of  $-0.75$ . The radio loudness based on  $\alpha = -0.5$  to  $-0.75$  increases 12%–15%. The radio loud fraction has no change.

Jiang et al. (2007) suggest that the RLF is a function of absolute magnitude  $M_{2500}$  and redshift at  $z < 4$ , and give the best fit for the function. To compare with Jiang et al. (2007), we also calculate the radio/optical flux density ratio  $R_{2500} = f_{\nu, 5 \text{ GHz}}/f_{\nu, 2500 \text{ Å}}$ , where  $f_{\nu, 2500 \text{ Å}}$  is the optical flux density at rest-frame 2500 Å. We convert  $M_{1450}$  to  $M_{2500}$  by  $M_{2500} = M_{1450} - 0.3$  on the assumption of an optical spectral index of approximately  $-0.5$ . For comparison, here we use the same cosmology as Jiang et al. (2007), which is  $H_0 = 70 \text{ km s}^{-1} \text{ Mpc}^{-1}$ ,  $\Omega_m = 0.3$ , and  $\Omega_\Lambda = 0.7$ . Our sample covers magnitudes of  $-27.03 < M_{2500} < -29.22$ . Due to the fact that there are only 8 quasars with radio detection covering a narrow redshift range, we use only one redshift bin and roughly divide our sample into two magnitude bins, one for  $M_{2500} < -28$  and the other one for  $M_{2500} > -28$ . Here we use  $R > 30$  as the definition of the radio loud quasar so that FIRST with limiting flux of  $\sim 1$  mJy will be deep enough for our quasar sample. NVSS, with an  $\sim 2.5$  mJy flux limit, is still not deep enough and is able to detect radio-loud quasars ( $R > 30$ ) at  $z \sim 5$  only down to  $M_{2500} \sim -27.7$ . Therefore, we calculate the RLF for quasars within the area covered by FIRST and NVSS, respectively. In the bright magnitude bin, there are 13 quasars in the FIRST coverage and 19 quasars in the NVSS coverage. In the faint bin, there are 68 quasars in the FIRST coverage and 80 quasars in the NVSS coverage. The details and radio loudness of radio detected quasars are given in Table 4. We compare our result with the RLF evolution

function  $\log(\text{RLF}/(1-\text{RLF})) = -0.218 - 2.096 \log(1+z) - 0.203(M_{2500} + 26)$  from Jiang et al. (2007). As shown in Figure 12, our points show an evolution of the RLF with magnitude, but prefer a higher RLF at  $z \sim 5$  than the prediction. Our result suggests that the RLF may evolve with optical luminosity, but it may not decline as rapidly with increasing redshift as measured in Jiang et al. (2007) at high redshift, though this could be affected by the small number of radio-loud quasars in our sample.

## 6. CONCLUSION

We establish a highly effective  $z \sim 5$  quasar selection method based on SDSS and ALLWISE optical/near-infrared colors. We relax the traditional  $r - i/i - z$  color limit by including color cuts in the ALLWISE W1 and W2 data. We selected 110 quasar candidates that satisfied our selection criteria with good optical image quality and obtained spectroscopic observations for 99 candidates. 64 new quasars have been discovered in the redshift range of  $4.4 < z < 5.5$  and magnitude range of  $-29 < M_{1450} < -26.4$ . We restrict our luminous quasar sample to  $4.7 \leq z < 5.4$  and  $M_{1450} \leq -26.8$  for the QLF calculation. Combining all previously known quasars in this range, we construct the largest luminous quasar sample at  $z \sim 5$  and determine the QLF, covering a sky area of  $14,555 \text{ deg}^2$ . Here we list our main conclusions.

1. Within the redshift range of  $4.7 \leq z < 5.4$  and magnitude range of  $M_{1450} \leq -26.8$ , there are 45 newly identified quasars and 54 known quasars. Our new discovery successfully extends the population of luminous quasars at  $z \sim 5$ , especially at  $M_{1450} \leq -27.3$ , where we discovered 27 new quasars and increased the number of known quasars by a factor of 1.5 in this luminosity range. Our final sample, including 99 quasars, is the largest sample of luminous  $z \sim 5$  quasars (Figure 1).
2. We derive the selection function of our color-color selection by using 311,000 simulated quasars in the redshift range of  $z = 4-6$  and luminosity range of  $-29.5 < M_{1450} < -25.5$ . The selection function shows that by relaxing the traditional  $r - i/i - z$  color cut and adding the W1 - W2 color, our color selection criteria extend the selection function to a higher redshift  $z \sim 5.4$  than previous work (Figure 5).
3. Using this sample, we calculate the binned QLF and fit the parametric QLF by using maximum likelihood fitting at  $z = 5.05$  (Figures 8 and 9). For the parametric QLF,



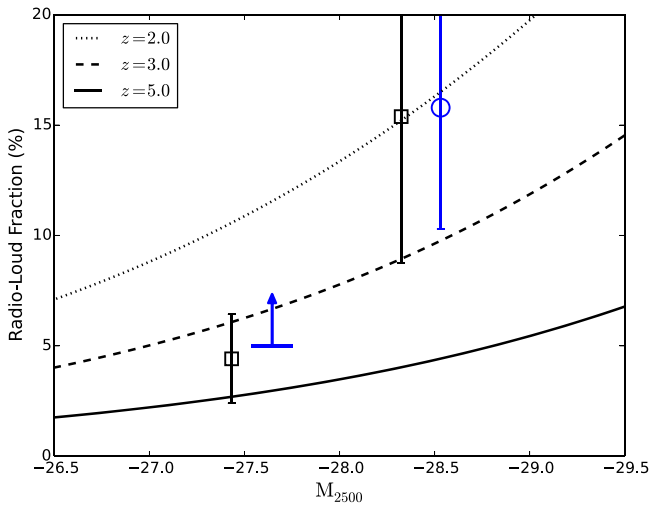


**Figure 12.** RLF in each magnitude bin compared with the evolution function from Jiang et al. (2007). The dotted, dashed, and solid lines show the predicted RLF at  $z = 2, 3$ , and  $5$  from Jiang et al. (2007). The black squares represent the RLF in the FIRST area, and the blue circle and blue arrow denote the result from quasars within the NVSS area. In the faint magnitude bin, the RLF based on NVSS data is a lower limit. To show the points clearly, we shift the NVSS points by  $-0.2$  mag. The uncertainties of RLF is estimated by assuming a poisson distribution of the number of quasars in each bin.

we fix the faint-end slope  $\alpha = -2.03$ , which is measured by using the S82 and DR7 quasar samples (M13), and find the best-fit result of the bright end slope  $\beta = -3.58 \pm 0.25$  and break magnitude of  $M_{1450}^* = -26.99 \pm 0.23$ .

4. We compare parameters of our best-fit QLF with previous work at different redshifts and use all points to fit an LEDE model. Our result is consistent with the previous LEDE model but prefers a steeper slope of  $\log \Phi^*(z)$  evolution and a flatter slope of break magnitude evolution. The comparison for  $\beta$  shows no clear evolution with redshift (Figure 11).
5. We calculate the contribution of quasars to the ionizing background at  $z \sim 5$  based on our QLF. Integrating our best-fit QLF, we find that quasars are able to provide  $\sim 18\%$ – $45\%$  of the required photons based on a clumping factor of  $C \sim 2$ – $5$ .
6. We use FIRST and NVSS data to calculate the radio loud fraction of our sample and give a lower limit for the RLF of  $\sim 7.1\%$ , which agrees with the result at  $z \sim 6$  of Bañados et al. (2015). In comparison to the predicted evolution function of the RLF with  $M_{2500}$  and  $z$  proposed by Jiang et al. (2007), our result shows evolution with optical luminosity but no obvious evolution with redshift (Figure 12).

We thank the referee for providing constructive comments and suggestions. J.Y., F.W., and X.-B.W. are thankful for support by NSFC grant Nos. 11373008 and 11533001, the Strategic Priority Research Program “The Emergence of Cosmological Structures” of the Chinese Academy of Sciences, grant No. XDB09000000, and the National Key Basic Research Program of China 2014CB845700, and support from the Ministry of Science and Technology of China under grant 2016YFA0400703. J.Y., X.F., and I.D.M. acknowledge the support from the US NSF grant AST 11-07682. Funding for the Lijiang 2.4 m telescope is provided by Chinese Academy of

Sciences and the People’s Government of Yunnan Province. This research uses data obtained through the Telescope Access Program (TAP), which has been funded by the Strategic Priority Research Program “The Emergence of Cosmological Structures” (grant No. XDB09000000), National Astronomical Observatories, Chinese Academy of Sciences, and the Special Fund for Astronomy from the Ministry of Finance in China. We acknowledge the use of the Lijiang 2.4 m telescope, the MMT 6.5 m telescope, the Bok telescope, the ANU 2.3 m telescope, and the Xinglong 2.16 m telescope. We acknowledge the support of the staff of the Xinglong 2.16 m telescope. This work was partially supported by the Open Project Program of the Key Laboratory of Optical Astronomy, National Astronomical Observatories, Chinese Academy of Sciences.

We acknowledge the use of SDSS photometric data. Funding for SDSS-III has been provided by the Alfred P. Sloan Foundation, the Participating Institutions, the National Science Foundation, and the U.S. Department of Energy Office of Science. The SDSS-III Web site is <http://www.sdss3.org/>. SDSS-III is managed by the Astrophysical Research Consortium for the Participating Institutions of the SDSS-III Collaboration including the University of Arizona, the Brazilian Participation Group, Brookhaven National Laboratory, University of Cambridge, Carnegie Mellon University, University of Florida, the French Participation Group, the German Participation Group, Harvard University, the Instituto de Astrofísica de Canarias, the Michigan State/Notre Dame/JINA Participation Group, Johns Hopkins University, Lawrence Berkeley National Laboratory, Max Planck Institute for Astrophysics, Max Planck Institute for Extraterrestrial Physics, New Mexico State University, New York University, Ohio State University, Pennsylvania State University, University of Portsmouth, Princeton University, the Spanish Participation Group, University of Tokyo, University of Utah, Vanderbilt University, University of Virginia, University of Washington, and Yale University. This publication makes use of data products from the *Wide-field Infrared Survey Explorer*, which is a joint project of the University of California, Los Angeles, and the Jet Propulsion Laboratory/California Institute of Technology, and NEOWISE, which is a project of the Jet Propulsion Laboratory/California Institute of Technology. WISE and NEOWISE are funded by the National Aeronautics and Space Administration.

*Facilities:* Sloan (SDSS), WISE, 2.4 m/YAO (YFOSC), MMT (Red Channel spectrograph), 2.16 m/NAOC (BFOSC), 2.3 m/ANU (WiFeS), Bok/Steward Observatory (B&C).

## REFERENCES

- Avni, Y., & Bahcall, J. N. 1980, *ApJ*, **235**, 694  
 Bañados, E., Venemans, B. P., Morganson, E., et al. 2015, *ApJ*, **804**, 118  
 Becker, G. D., Bolton, J. S., Madau, P., et al. 2015, *MNRAS*, **447**, 3402  
 Becker, R. H., White, R. L., & Helfand, D. J. 1995, *ApJ*, **450**, 559  
 Bolton, J. S., Becker, G. D., Raskutti, S., et al. 2012, *MNRAS*, **419**, 2880  
 Bolton, J. S., & Haehnelt, M. G. 2007, *MNRAS*, **382**, 325  
 Bongiorno, A., Zamorani, G., Gavignaud, I., et al. 2007, *A&A*, **472**, 443  
 Boroson, T. A., & Green, R. F. 1992, *ApJS*, **80**, 109  
 Boyle, B. J., Shanks, T., Croom, S. M., et al. 2000, *MNRAS*, **317**, 1014  
 Brown, M. J. I., Brand, K., Dey, A., et al. 2006, *ApJ*, **638**, 88  
 Cirasuolo, M., Magliocchetti, M., Celotti, A., & Danese, L. 2003, *MNRAS*, **341**, 993  
 Condon, J. J., Cotton, W. D., Greisen, E. W., et al. 1998, *AJ*, **115**, 1693  
 Croom, S. M., Richards, G. T., Shanks, T., et al. 2009, *MNRAS*, **399**, 1755  
 Croom, S. M., Smith, R. J., Boyle, B. J., et al. 2004, *MNRAS*, **349**, 1397  
 Fan, X. 1999, *AJ*, **117**, 2528



- Fan, X., Carilli, C. L., & Keating, B. 2006, *ARA&A*, **44**, 415
- Fan, X., Narayanan, V. K., Lupton, R. H., et al. 2001a, *AJ*, **122**, 2833
- Fan, X., Strauss, M. A., Schneider, D. P., et al. 1999, *AJ*, **118**, 1
- Fan, X., Strauss, M. A., Schneider, D. P., et al. 2001b, *AJ*, **121**, 54
- Finlator, K., Oh, S. P., Özel, F., & Davé, R. 2012, *MNRAS*, **427**, 2464
- Glikman, E., Bogosavljević, M., Djorgovski, S. G., et al. 2010, *ApJ*, **710**, 1498
- Glikman, E., Helfand, D. J., & White, R. L. 2006, *ApJ*, **640**, 579
- Goldschmidt, P., Kukula, M. J., Miller, L., & Dunlop, J. S. 1999, *ApJ*, **511**, 612
- Hooper, E. J., Impey, C. D., Foltz, C. B., & Hewett, P. C. 1995, *ApJ*, **445**, 62
- Ivezić, Ž., Menou, K., Knapp, G. R., et al. 2002, *AJ*, **124**, 2364
- Jiang, L., Fan, X., Annis, J., et al. 2008, *AJ*, **135**, 1057
- Jiang, L., Fan, X., Cool, R. J., et al. 2006, *AJ*, **131**, 2788
- Jiang, L., Fan, X., Ivezić, Ž., et al. 2007, *ApJ*, **656**, 680
- Kashikawa, N., Ishizaki, Y., Willott, C. J., et al. 2015, *ApJ*, **798**, 28
- Kellermann, K. I., Sramek, R., Schmidt, M., Shaffer, D. B., & Green, R. 1989, *AJ*, **98**, 1195
- Komatsu, E., Dunkley, J., Nolte, M. R., et al. 2009, *ApJS*, **180**, 330
- Kratzer, R. M., & Richards, G. T. 2015, *AJ*, **149**, 61
- Kuhn, O., Elvis, M., Bechtold, J., & Elston, R. 2001, *ApJS*, **136**, 225
- La Franca, F., Gregorini, L., Cristiani, S., de Ruiter, H., & Owen, F. 1994, *AJ*, **108**, 1548
- Lampton, M., Margon, B., & Bowyer, S. 1976, *ApJ*, **208**, 177
- Laor, A. 2000, *ApJL*, **543**, L111
- Lupton, R. H., Gunn, J. E., & Szalay, A. S. 1999, *AJ*, **118**, 1406
- Madau, P., Haardt, F., & Rees, M. J. 1999, *ApJ*, **514**, 648
- Marshall, H. L., Tananbaum, H., Avni, Y., & Zamorani, G. 1983, *ApJ*, **269**, 35
- Masters, D., Capak, P., Salvato, M., et al. 2012, *ApJ*, **755**, 169
- McGreer, I. D., Helfand, D. J., & White, R. L. 2009, *AJ*, **138**, 1925
- McGreer, I. D., Jiang, L., Fan, X., et al. 2013, *ApJ*, **768**, 105
- McGreer, I. D., Mesinger, A., & D’Odorico, V. 2015, *MNRAS*, **447**, 499
- McQuinn, M., Oh, S. P., & Faucher-Giguère, C.-A. 2011, *ApJ*, **743**, 82
- Meiksin, A. 2005, *MNRAS*, **356**, 596
- Padovani, P. 1993, *MNRAS*, **263**, 461
- Page, M. J., & Carrera, F. J. 2000, *MNRAS*, **311**, 433
- Päris, I., Petitjean, P., & Ross, N. P. 2016, arXiv:1608.06483
- Rees, M. J., Begelman, M. C., Blandford, R. D., & Phinney, E. S. 1982, *Natur*, **295**, 17
- Richards, G. T., Croom, S. M., Anderson, S. F., et al. 2005, *MNRAS*, **360**, 839
- Richards, G. T., Fan, X., Newberg, H. J., et al. 2002, *AJ*, **123**, 2945
- Richards, G. T., Strauss, M. A., Fan, X., et al. 2006, *AJ*, **131**, 2766
- Ross, N. P., McGreer, I. D., White, M., et al. 2013, *ApJ*, **773**, 14
- Schmidt, M. 1968, *ApJ*, **151**, 393
- Schneider, D. P., Richards, G. T., Hall, P. B., et al. 2010, *AJ*, **139**, 2360
- Schneider, D. P., Schmidt, M., & Gunn, J. E. 1991, *AJ*, **102**, 837
- Selsing, J., Fynbo, J. P. U., Christensen, L., & Krogager, J.-K. 2016, *A&A*, **585**, A87
- Shull, J. M., Harness, A., Trenti, M., & Smith, B. D. 2012, *ApJ*, **747**, 100
- Songaila, A., & Cowie, L. L. 2010, *ApJ*, **721**, 1448
- Stern, D., Djorgovski, S. G., Perley, R. A., de Carvalho, R. R., & Wall, J. V. 2000, *AJ*, **119**, 1526
- Stevens, M. L., Shull, J. M., Danforth, C. W., & Tilton, E. M. 2014, *ApJ*, **794**, 75
- Tsuzuki, Y., Kawara, K., Yoshii, Y., et al. 2006, *ApJ*, **650**, 57
- Vanden Berk, D. E., Richards, G. T., Bauer, A., et al. 2001, *AJ*, **122**, 549
- Vestergaard, M., & Wilkes, B. J. 2001, *ApJS*, **134**, 1
- Wang, F., Wu, X.-B., Fan, X., et al. 2016, *ApJ*, **819**, 24 (Paper I)
- Willott, C. J., Delorme, P., Reylé, C., et al. 2010, *AJ*, **139**, 906
- Wilson, A. S., & Colbert, E. J. M. 1995, *ApJ*, **438**, 62
- Wolf, C., Wisotzki, L., Borch, A., et al. 2003, *A&A*, **408**, 499
- Worseck, G., & Prochaska, J. X. 2011, *ApJ*, **728**, 23
- Wright, E. L., Eisenhardt, P. R. M., Mainzer, A. K., et al. 2010, *AJ*, **140**, 1868
- Yip, C. W., Connolly, A. J., Vanden Berk, D. E., et al. 2004, *AJ*, **128**, 2603
- Yuan, H., Zhang, H., Zhang, Y., et al. 2013, *A&C*, **3**, 65